ISSN 1063-7834, Physics of the Solid State, 2017, Vol. 59, No. 7, pp. 1321–1331. © Pleiades Publishing, Ltd., 2017.
Original Russian Text © V.G. Pushin, E.B. Marchenkova, A.V. Korolev, N.I. Kourov, E.S. Belosludtseva, A.V. Pushin, A.N. Uksusnikov, 2017, published in Fizika Tverdogo Tela, 2017, Vol. 59, No. 7, pp. 1297–1306.

MAGNETISM

Magnetically Controlled Thermoelastic Martensite Transformations and Properties of a Fine-Grained $Ni_{54}Mn_{21}Ga_{25}$ Alloy

V. G. Pushin[a, b, *], E. B. Marchenkova[a], A. V. Korolev[a, b], N. I. Kourov[a], E. S. Belosludtseva[a], A. V. Pushin[a], and A. N. Uksusnikov[a]

[a] *Institute of Metal Physics, Ural Branch, Russian Academy of Sciences, ul. S. Kovalevskoi 18, Yekaterinburg, 620990 Russia*

[b] *Ural Federal University, ul. Mira 19, Yekaterinburg, 620002 Russia*

**e-mail: pushin@imp.uran.ru*

Received October 25, 2016

Abstract—Comparative studies of physical characteristics (the electrical resistivity, the magnetic susceptibility, the magnetization, the bending deformation, and the degree of shape recovery during subsequent heating) of the $Ni_{54}Mn_{21}Ga_{25}$ ferromagnetic alloy as-cast and rapidly quenched from melt have been performed in the temperature range 2–400 K. The results are compared to the results of studying the structural–phase transformations by transmission and scanning electron microscopy and X-ray diffraction. It is found that the rapid quenching influences the microstructure, the magnetic state, the critical temperatures, and the specific features of thermoelastic martensite transformations in the alloy. It is found that the resource of the alloy plasticity and thermomechanical bending cyclic stability demonstrates a record-breaking increase in the intercritical temperature range and during subsequent heating.

DOI: 10.1134/S1063783417070198

1. INTRODUCTION

Alloys based on intermetallic compounds NiTi ($Ni_{50}Ti_{50}$) and Ni_2MnGa ($Ni_{50}Mn_{25}Ga_{25}$; the component contents are given in at %) are of continuous interest for researchers due to a variety of the structural and phase transformations upon cooling, heating, and under load and, as a result, their high innovation potential [1–4]. Like many alloys with thermoelastic martensite transformations (TMT), the phase transformations in these alloys are preceded by a clear pretransition softening of the elastic moduli and the softening of some phonon modes [1–8]. A substantial result of TMT in these alloys is the existence of the shape memory effects (SME) that can be controlled in Ni_2MnGa-type ferromagnets by external magnetic field [4], unlike the case of other, for example, titanium nickelide-based alloys [1–3].

The $Ni_{50}Mn_{25}Ga_{25}$-based $L2_1$ Heusler alloys undergo subsequent structural martensite transformations to phases with symmetries lower than $L2_1$ [9]. The martensite phases can exhibit different structures and have not only the tetragonal but also long-periodic, orthorhombic, or monoclinically distorted lattices [10–12]. In this case, the main most intense structural reflections and weaker extrareflections are studied using different diffraction methods. The interpretation of extrareflections that are located nearly equidistantly along certain directions of the reciprocal lattice allows their ambiguous description: they can be interpreted as the manifestation of the formation of a substructure modulated by periodic shifts over the (110) $[1\,\bar{1}0]$ system in the $L2_1$ lattice or as a result of the formation of new practically commensurable phases with a long-periodic almost five-fold or seven-fold laying of the initial close-packed (110) $L2_1$ planes. This martensite is denoted as the $(3\bar{2})$-type five-layer or $5M$ martensite or the $(5\bar{2})$-type seven-layer or $7M$ martensite [10–12]. In the case of another choice of the description of the crystal lattice type, these martensite phases are denoted as $10M$ and $14M$, respectively.

One more phase can form during TMT under mechanical load, namely, body-centered tetragonal (bct) martensite phase, the degree of tetragonality of which is $c/a \sim 1.2$ and the direction of axis c during a deformation of the $Ni_{50}Mn_{25}Ga_{25}$ single crystal is stated along the extension axis or perpendicularly to the contraction axis [13]. The same nonmodulated bct phase (NM), the tetragonality of which varies within $c/a \sim 1.18$–1.23, depending on the chemical composition, can form in the nonstoichiometric alloys on their cooling [12].

It is known from the structural neutron diffraction [9] that the austenite high-temperature phase in the stoichiometric $Ni_{50}Mn_{25}Ga_{25}$ intermetallic compound that is a prototype of the alloy studied in this work has

the atomically-ordered Heusler-type crystal $L2_1$ superstructure. The structure of nonstoichiometric alloys based on this compound was less well understood, and it was studied using mainly X-ray diffraction and electron diffraction. The type and the degree of atomic ordering of the alloys in the high-temperature state and their influence on TMT and SME remain incompletely understood, since the atomic scattering factors of the chemical elements composing the alloys are close to each another [4, 9, 14]. The real structures of these alloys in the case of using the synthesis methods and external actions which lead to substantially nonequilibrium states are also less understood [4, 13, 14].

The nonstoichiometric $Ni_{54}Mn_{21}Ga_{25}$ alloy occupies a specific place among $Ni_{50}Mn_{25}Ga_{25}$-based ferromagnetic alloys that exhibit magnetically controlled SME [15–20]. Its start and final temperatures of the direct (M_s, M_f) and inverse (A_s, A_f) TMTs that determine SME and the Curie temperature T_C are close to room temperature, and this is convenient in cases of its study and also its possible practical application. In turn,

a technology of rapid quenching from melt (RQM) is first interesting due to the quest to form more plastic ultrafine-grained states in the alloys, since the extremely high brittleness is a catastrophic disadvantage of usual as-cast coarse-grained alloys of this system [21]. Because of this, in this work, we performed a comparative study of the structure and physical properties of the as-cast ferromagnetic $Ni_{54}Mn_{21}Ga_{25}$ alloy produced in the initial atomically ordered state with the $L2_1$ crystal lattice and the RQM alloy with the same chemical composition.

2. EXPERIMENTAL

The $Ni_{54}Mn_{21}Ga_{25}$ alloy with nominal composition (at %) was produced by arc melting in an inert atmosphere on a water-cooled copper hearth. The initial components were high-purity metals (99.99% pure). The alloy ingots were subjected to a long-term homogenizing annealing; then, platelike samples intended for the measurements of the physical properties and for structural-phase studies were cut from the ingots using the electric-spark method.

The rapid cooling was performed in an inert atmosphere by spinning of the melt jet on a rapidly rotating copper cylinder at a cooling rate of 10^5 K/s; as a result, we obtained samples as thin (40 μm in thickness) and quite plastic ribbons (the chemical composition is given in Table 1), unlike the brittle samples of the initial as-cast alloy with the same integral chemical composition.

The alloys were studied in the initial as-cast state, after RQM, and after annealing.

Table 1. Chemical composition of the $Ni_{54}Mn_{21}Ga_{25}$ RQM alloy

Element	Content	
	wt %	at %
Mn	18.89	20.87
Ni	52.21	53.97
Ga	28.90	25.16

The electrical resistance was measured using a doubled bridge scheme; the magnetic susceptibility and the magnetization were measured over a wide temperature range (2–400 K) using a VSM (LAKE SHORE) vibrating-coil magnetometer and a Quantum Design MPMS-5*XL* SQUID magnetometer. We also measured the bending deformation of the samples and the degree of recovery of their shapes due to SME on heating.

The electron-microscopy studies were carried out using a JEOL JEM-200CX, Tecnai G^2 30, and FEI CM 30 transmission electron microscopes (TEM), and also FEI Quanta-200 Pegasus scanning electron microscope (SEM) equipped with systems of energy-dispersive analysis and the analysis by backscattered electron diffraction. The X-ray diffraction studies were performed using a DRON-3M diffractometer in monochromatized CuK_α radiation.

3. ELECTRICAL CONDUCTIVITY OF THE ALLOYS

The resistivity ρ of the alloy was higher than 120 μΩ cm at temperatures higher than room temperature (T are higher than A_f and T_C) and was weakly dependent on its microstructure state (as-cast or after RQM). In the paramagnetic state, $\rho(T)$ was mainly determined by the phonon and magnetic components which are almost independent on the method of preparing the alloys in conditions fairly close to their Curie points and Debye temperatures, and also the magnetic moment μ_{eff} [22, 23]. Conversely, at low temperatures (T are much lower than M_f and T_C) the resistivity is first due to the conduction electron scattering by nonuniformities of the Coulomb potential in the crystal, i.e., it is determined by the degree of atomic order and the structure imperfection. Because of this, residual resistivity ρ_0 of the sample of the initial atomically ordered $Ni_{54}Mn_{21}Ga_{25}$ alloy was significantly (by a factor of approximately four) lower than ρ_0 of the rapidly quenched and, thus, partially disordered alloy of the same chemical composition.

It is seen from Figs. 1a, 1b, and 2 that dependences $\rho(T)$, like $\chi(T)$, were substantially changed near the TMT temperatures in the dependence on the alloy synthesis conditions. The $\rho(T)$ curves of the RQM alloy measured on cooling and heating in a fairly nar-

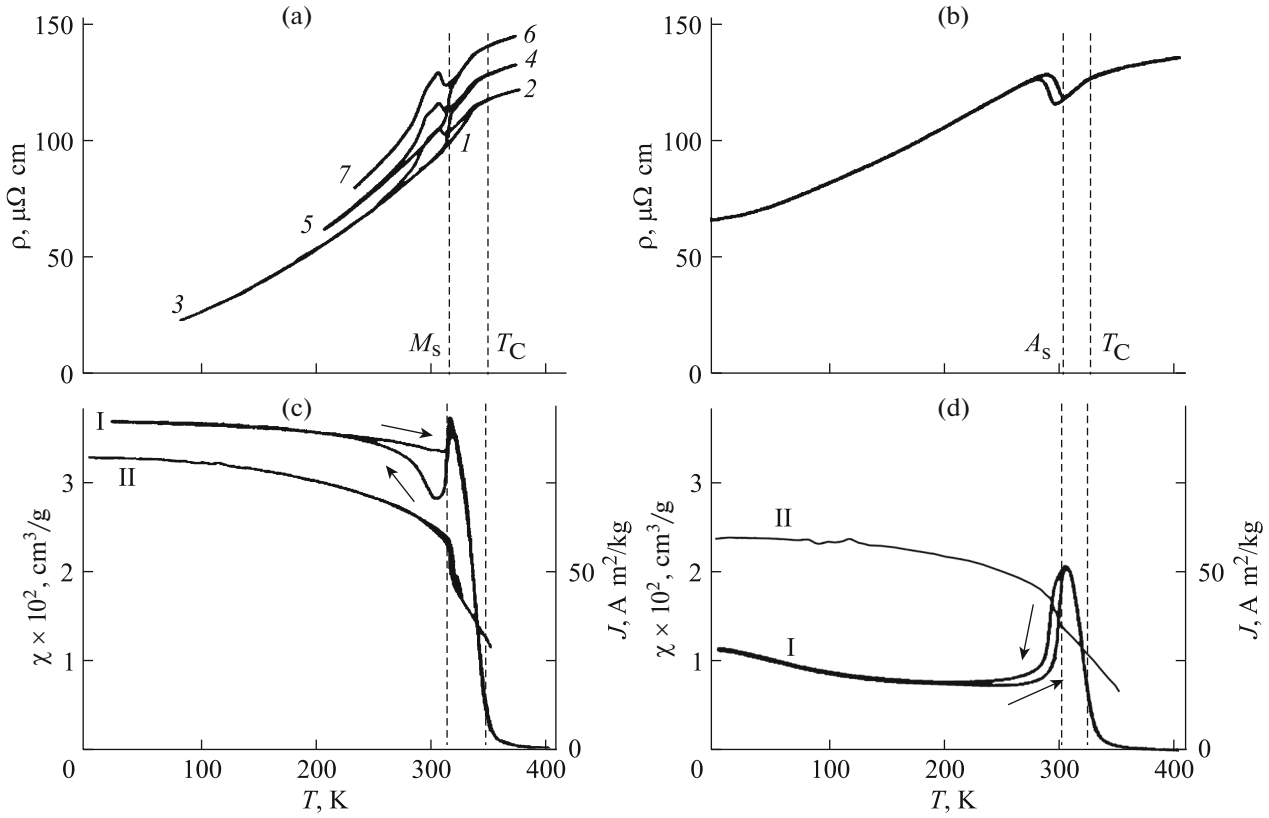

Fig. 1. Temperature dependences of resistivity $\rho(T)$, susceptibility $\chi(T)$ (I) and magnetization $J(H)$ (II) of the (a, c) initial as-cast and (b, d) rapidly quenched alloys; magnetization J was measured at $H = 4$ MA/m and susceptibility $\chi(T)$ at $H = 79.6$ kA/m. The sequence of the measurement cycles for $\rho(T)$ of the as-cast alloy is denoted by numerals *1*–*7*.

row temperature range demonstrated a hysteresis that was completely reproducible during repeated heating–cooling cycles of the sample (Fig. 1b). In this case, the resistivity in the martensite phase (at the end of the jump in curve $\rho(T)$ at $T < M_f$ or A_s) were always higher than that in the austenite phase (at temperatures that were slightly higher than M_s or A_f).

The hysteresis of curves $\rho(T)$ for the initial as-cast alloy had a more complex shape, and the temperature range in which it was observed was significantly larger than that in the rapidly quenched alloy (Fig. 1a). As is seen from Fig. 1, as the temperature of the as-cast alloy decreased, the resistivity also increased almost stepwise in the TMT point M_s, and, then, curve $\rho(T)$ sloped down and had two kinks that can be interpreted as the start and the final of the second martensite–martensite transformation. On heating, the resistivity ρ increased with temperature; however, $\rho(T)$ of the initial alloy (unlike that of the RQM alloy) did not decrease during the phase transition from the martensitic to the austenitic phase, but almost stepwise increased (in a narrow temperature range), and the value of the jump in $\rho(T)$ in the M_s–M_f range was smaller on cooling than that on heating in the A_s–A_f range, and the positions of the jumps in curve $\rho(T)$ in the temperature axis did not coincide in these two cases, forming, thus, the hysteresis. This led to that each cooling–heating cycle was accompanied by an irreversible increase in the resistivity of the initial alloy

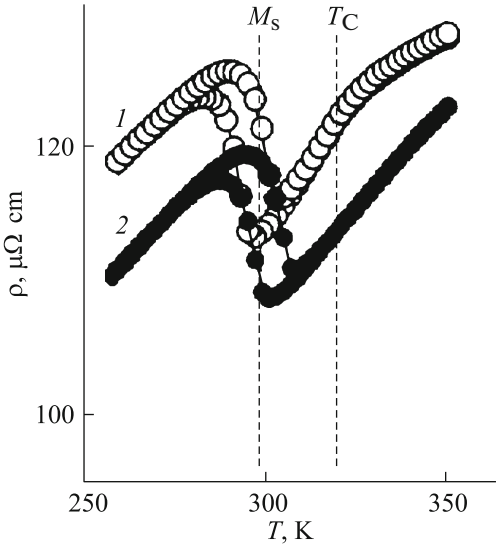

Fig. 2. Temperature dependence of resistivity $\rho(T)$ of the $Ni_{54}Mn_{21}Ga_{25}$ RQM alloy measured (*1*) in a zero magnetic field and (*2*) in field $H = 7.17$ MA/m.

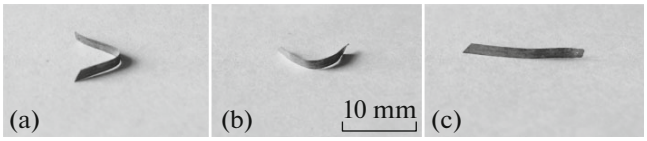

Fig. 3. Photography of the RQM ribbon during thermomechanical tests for realization of SME: (a) bending of the straight-line ribbon to a C-like shape at room temperature; (b) a partial spontaneous straightening of the ribbon on heating in the intercritical temperature range; (c) full straightening of the sample on heating for completion of TMT.

(Fig. 1a). Such an anomalous behavior of $\rho(T)$ of the as-cast $Ni_{54}Mn_{21}Ga_{25}$ alloy can be evidently explained by only progressing mechanical failure of the sample due to the formation of the continuity violation (microcracks) in it as a result of subsequent direct and inverse TMT, which was confirmed as the sample surface was studied after the measurement of $\rho(T)$.

The measured data on $\rho(T)$ were used to determine the TMT critical temperatures, the intervals between them, and the TMT hysteresis (Tables 2, 3). We should focus our attention on the fact that these temperatures increased by 4–8 K in a high magnetic field $H = 7.17$ MA/m, as compared to the temperatures of the initial RQM alloy (Fig. 2).

4. MAGNETIC PROPERTIES OF THE ALLOYS

Figures 1c, 1d, and 2 show the results of the measurements of magnetic susceptibility χ, magnetization J, and also resistivity ρ in magnetic field. It is seen that, in the RQM alloy, the magnetization $J(H)$ at $H =$ 4 MA/m and, correspondingly, the magnetic moment measured at $T = 2$ K decreased by a factor of approximately 1.5 (Fig. 1d). At low temperatures, the low-field ($H < 80$ kA/m) magnetic susceptibility decreased by a factor of ~3. The noted changes in the magnetic properties demonstrated the appearance of competing ferromagnetic and antiferromagnetic interactions in the $Ni_{54}Mn_{21}Ga_{25}$ RQM alloy.

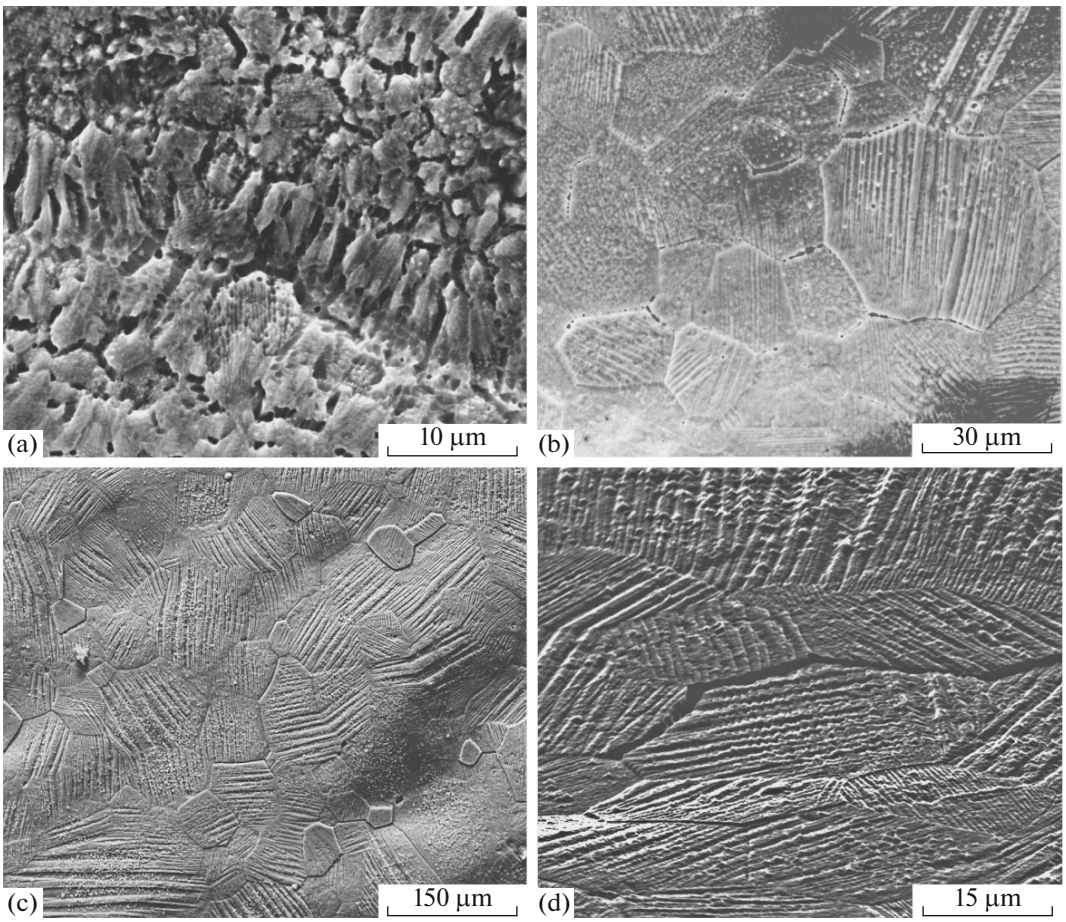

Fig. 4. SEM images of the $Ni_{54}Mn_{21}Ga_{25}$ RQM alloy in (a) the initial state, (b) after annealing at 1073 K for 5 h, and (c, d) after annealing at 1073 K for 72 h.

Table 2. Critical start and final temperatures of the direct and inverse TMTs in the as-cast and RQM $Ni_{54}Mn_{21}Ga_{25}$ alloys in the dependence on magnetic field H

Type of alloy	M_s, K	M_f, K	A_s, K	A_f, K	T_C, K
As-cast, $H \approx 0$	315	280	315	335	356
RQM, $H \approx 0$	294	286	290	302	329
RQM, $H \approx 7.17$ MA/m	298	290	298	306	–

Table 3. Temperature ranges of realization of the direct and inverse TMTs in the as-cast and RQM $Ni_{54}Mn_{21}Ga_{25}$ alloys in the dependence on magnetic field H

Type of alloy	$M_s - M_f$, K	$A_f - A_s$, K	$M_s - A_s$, K	$A_f - M_f$, K	$A_s - M_f$, K	$A_f - M_s$, K	ΔT,* K
As-cast, $H \approx 0$	35	20	0	55	35	20	27
RQM, $H \approx 0$	8	12	4	16	4	8	6
RQM, $H \approx 7.17$ MA/m	8	8	0	16	8	8	8

*$\Delta T = \{(A_f + A_s) - (M_s + M_f)\}/2$.

The magnetic characteristics of the $Ni_{54}Mn_{21}Ga_{25}$ RQM alloy were also substantially different in the vicinity of the temperatures of the magnetic and structural transformations as a result of some atomic disordering. It is seen from the comparison of Figs. 1c and 1d that the shapes of the hystereses of curves $\chi(T)$

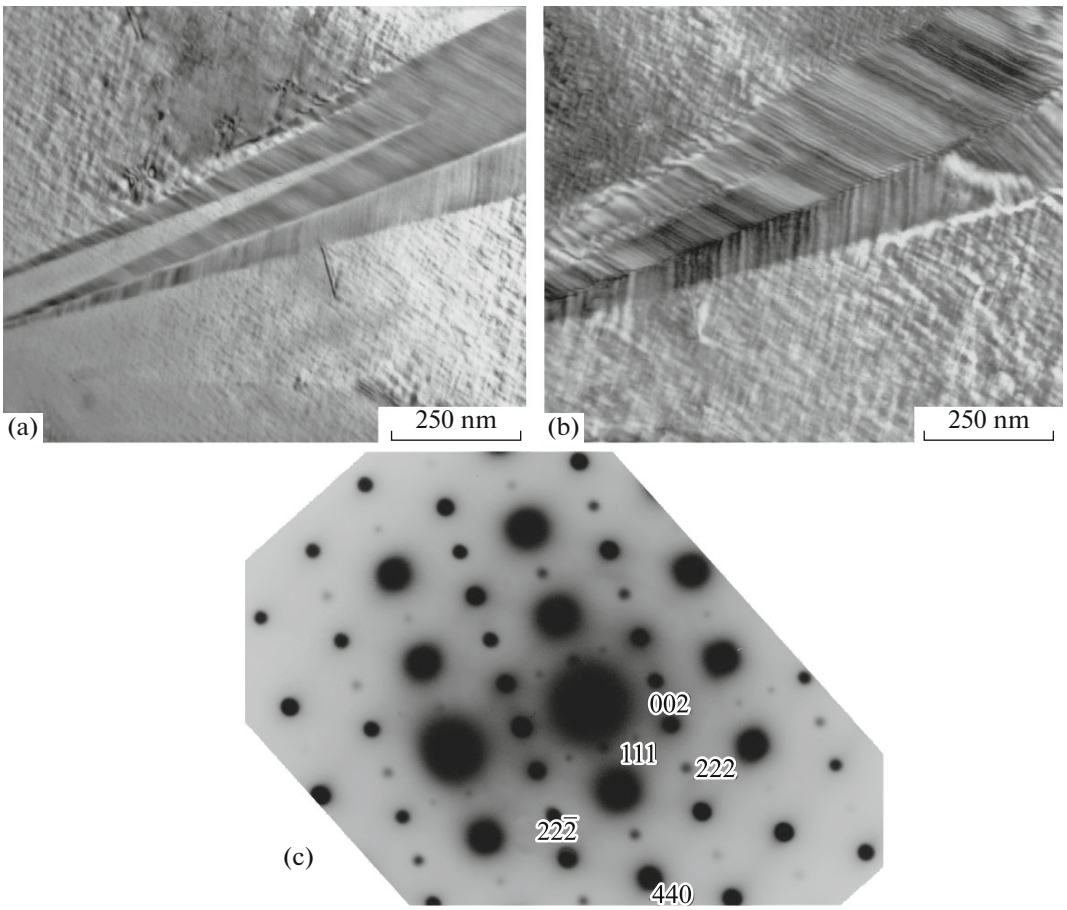

Fig. 5. (a, b) TEM images and (c) corresponding electron diffraction pattern of the as-cast alloy.

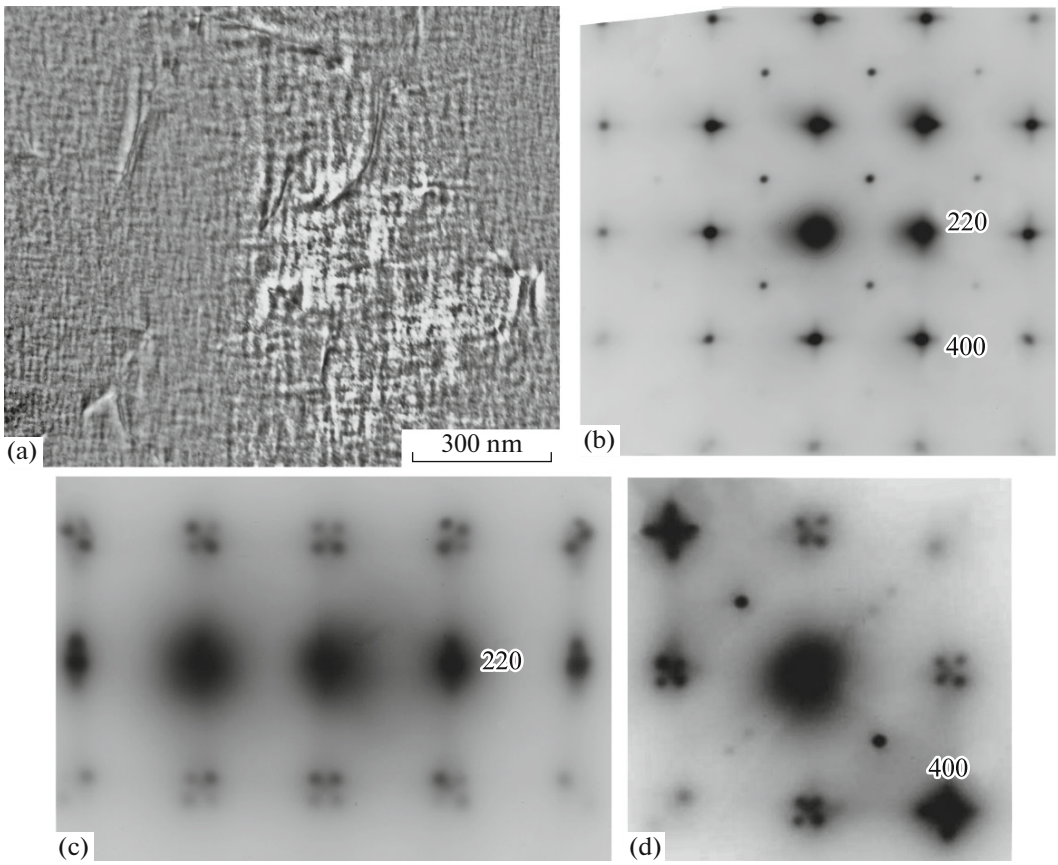

Fig. 6. (a) TEM image and (b–d) corresponding electron diffraction patterns of the $L2_1$ austenite of the RQM alloy.

measured in the RQM alloy on cooling and on heating of the samples were cardinally changed. In this case, the temperature range in which the hysteresis of $\chi(T)$ was observed decreased and the TMT temperatures M_s, A_s, and A_f slightly decreased, while, conversely, temperature M_f increased.

According to [14], the decrease in the Curie temperature observed in the $Ni_{54}Mn_{21}Ga_{25}$ RQM alloy (Table 2) can be due to the appearance of nonmagnetic Ga atoms in the nearest environment of the main magnetically active Mn atom. The practical absence of the change in the value of μ_{eff} (4.38 and 4.36μ_B/f.u., where μ_B is the Bohr magneton) observed in this case in conditions of a sharp increase in ratio μ_{eff}/μ_s (where μ_s is the spontaneous magnetic moment) at partial atomic and structural disordering of the alloy indicated the determining influence of competing ferromagnetic and antiferromagnetic interactions on the value and the process of magnetization in high magnetic fields.

The comparison of temperature dependences $\rho(T)$ measured in a zero magnetic field and at $H = 7.17$ MA/m clearly demonstrated that the applied magnetic field led to increase in the TMT temperatures M_s, M_f, and A_f by 4 K and A_s by 8 K (curves in Fig. 2).

5. MECHANICAL BEHAVIOR OF THE ALLOYS

The ribbon RQM samples with thickness $t = 40$ μm and 10–15 mm long were deformed on cylindrical mandrels with diameter $D = 2$ mm by 180° bending (the bending value was $\gamma = 100\%$ $t/D = 2\%$) at room temperature and then were heated to organize SME (Fig. 3). Even 3000 of such deformation–heating–cooling cycles did not fracture the samples, and the degree of recovery of their *C*-like shape to a straight-line shape was nearly 100%. The RQM ribbons demonstrated much higher thermomechanical cyclic stability after annealing at 1073 K. We failed to carry out similar experiments on the samples of the initial as-cast alloy, because of their brittle fracture even at bending by 0.5°–1.0°.

6. PHASE AND STRUCTURAL TRANSFORMATIONS IN THE ALLOYS

Consider the results of the structural studies performed in this work. According to the SEM data, the

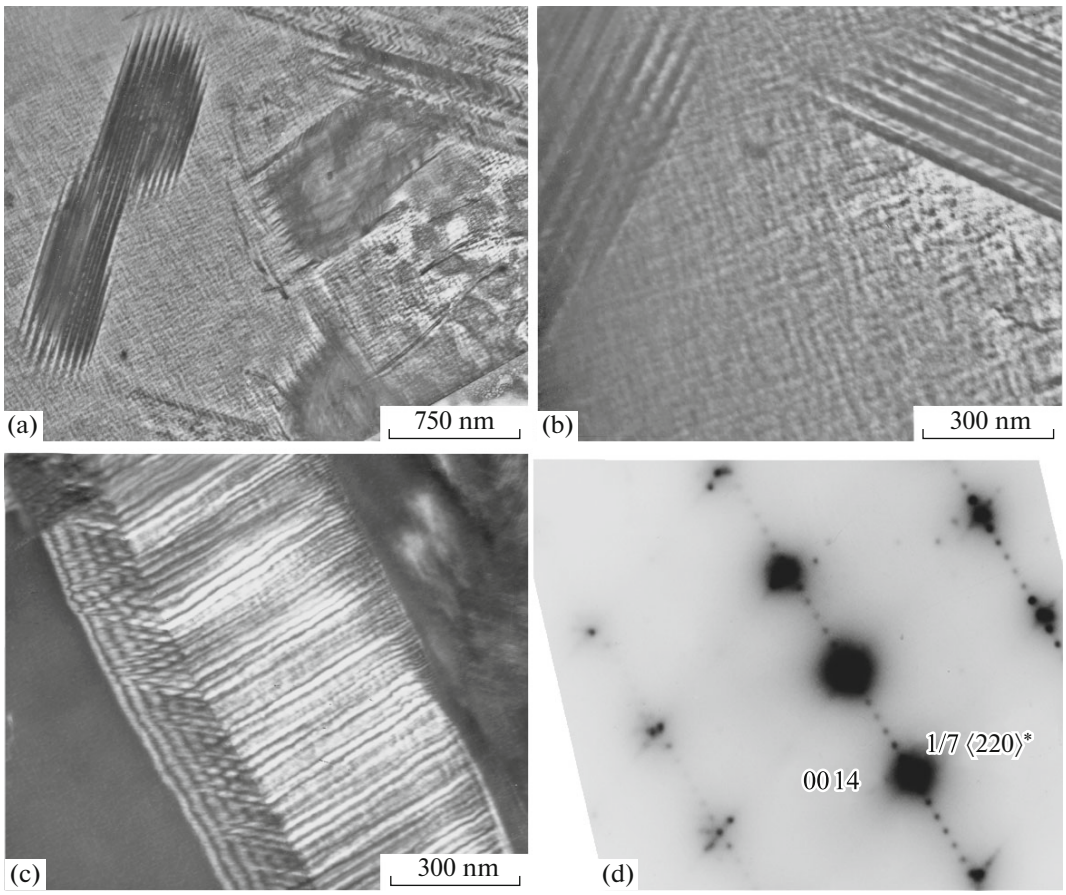

Fig. 7. (a–c) TEM images and (d) corresponding electron diffraction pattern of the long-periodic martensite of the as-cast alloy obtained at (a, b) room temperature and (c, d) 170 K.

average size of almost equiaxial grains in the $Ni_{54}Mn_{21}Ga_{25}$ RQM alloy was several micrometers (Fig. 4a). This is 500–1000 times smaller than the grain size in the initial as-cast alloy, in which the grains had very large scatters in size, morphology, and chemical composition because of their liquation during solidification that led to its fluctuation from the nominal composition by 0.5–1.0 at %.

TEM of the electrolytically thinned foils was performed by the in situ method in the goniometric holders that allowed heating and cooling in the microscope column. It was found that the high-temperature austenite phase in the alloy had the $L2_1$ ordered crystal structure as demonstrated by the 111 and 002 superstructure reflections observed on the electron diffraction patterns (Fig. 5c). In this case, the TEM images of the austenite obtained at room temperature and on in situ heating demonstrated a tweed diffraction contrast of the deformation origin. It was formed by characteristic contrast elements with sizes from 1 to 10 nm in the dependence on the slopes of the samples, which were oriented along the traces of intersecting the {110} $L2_1$-type planes with the foil surface (Figs. 5, 6) The tweed contrast intensity was dependent on the acting reflection (compare Figs. 5a and 5b) and it slightly decreased on heating, according to visual estimations. This contrast had the maximum intensity on the extinction contours.

A specific feature of the electron diffraction patterns of the $L2_1$ austenite was the existence of extended diffusion scattering effects as off-radial traces that were the traces of intersection of the Ewald sphere with diffusion layers located along planes {111}* of the reciprocal lattice $L2_1$ [1–3]. Most intense off-radial traces in directions ⟨110⟩* were observed near the structural reflections (Figs. 6b–6d). An important peculiarity of this diffusion electron scattering was the presence of the intensity amplifications disposed on the traces along directions ⟨110⟩* in positions 1/6⟨220⟩* (or 1/3⟨110⟩*) (Fig. 6). They were observed more clearly at temperatures lower than T_C, but also observed in the paramagnetic austenite. These data agreed well with the neutron diffraction data [6, 7]. Figure 6 shows the electron diffraction patterns with the axis of the zone of reflecting [001]$L2_1$ planes in (b) the exact position and after the foil slope by several

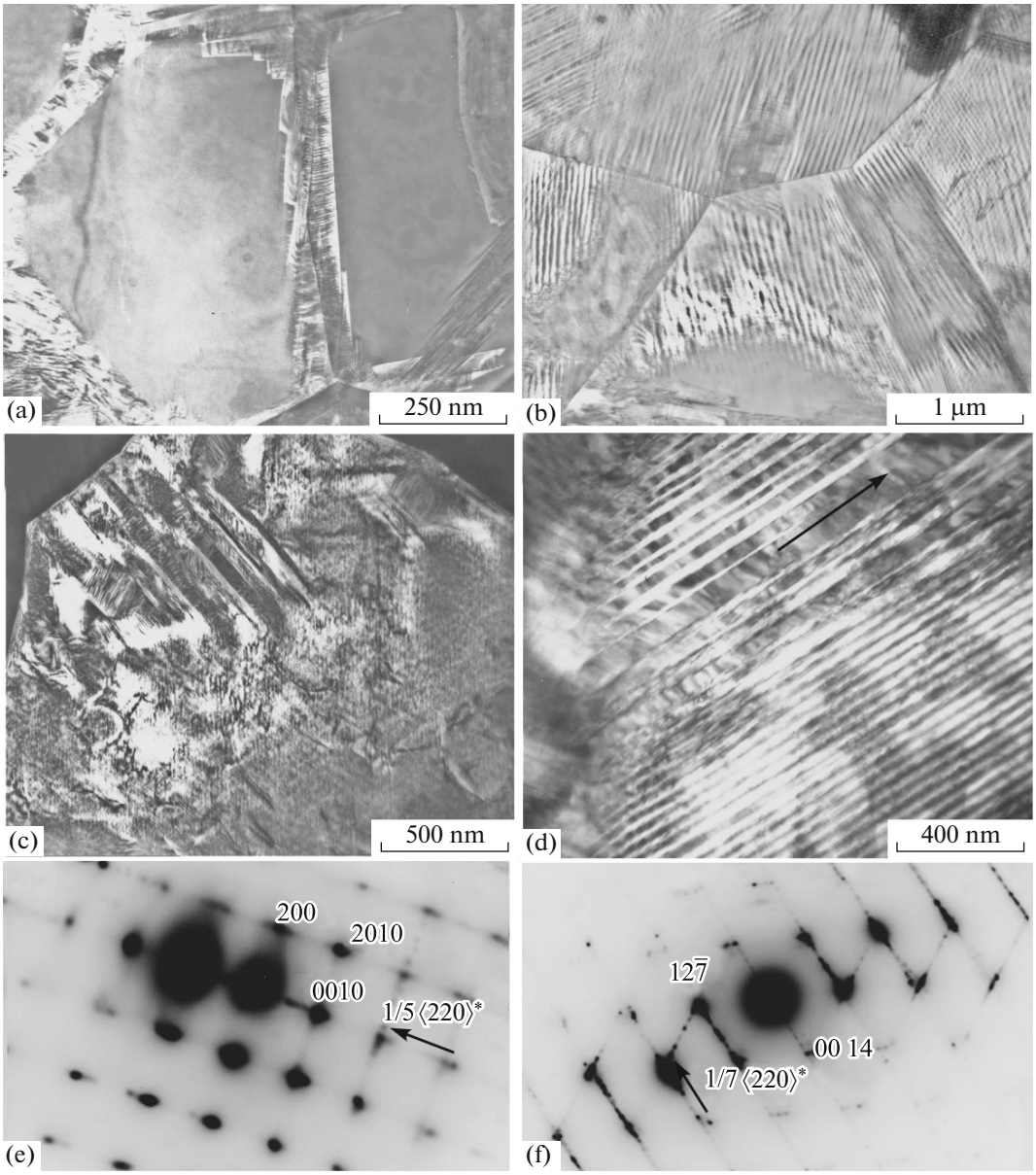

Fig. 8. TEM images and corresponding electron diffraction patterns of the RQM alloy obtained at (a, c, e) room temperature and (b, d, f) 170 K.

degrees by rotation around (c) axis [110] or (d) axis [100]. In these three cases, the two latter electron diffraction patterns contained "fours" and "twos" of the extrareflections rotated at an angle of 45° to the ⟨110⟩*-type direction, along with the off-radial diffusion traces lying in the plane of the electron diffraction pattern and the amplifications on the traces in the 1/3⟨110⟩* positions. The origin of these extrareflections was related to "the punctures" of the Ewald scattering sphere by intense traces along ⟨110⟩* that did not belong to given section of the reciprocal lattice. These diffraction data fairly completely described the nanodomain premartensite state in the initial mean $L2_1$ lattice, in which the displacement of atoms were described by the modulation of the threefold wave of transverse displacements $3 \times (110)[\bar{1}10]$ [1–4] and correlated well with the neutron diffraction measurements of the soft-mode behavior of $Ni_{50}Mn_{25}Ga_{25}$ alloys [6, 7].

At room temperature, the as-cast alloy, as well as the RQM alloy, was in a two-phase austenite–martensite state (Figs. 5a, 5b and 7a, 7b). Lamellar and acute-angled martensite crystals were arranged, as a rule, at an angle to the foil surface and had a fine-twin substructure parallelly to one of families of the $\{110\}L2_1$

planes. The habits of the crystals and the microtwins were close to $\{110\}L2_1$. The electron diffraction patterns contained extrareflections along the diffusion traces in positions $1/5\langle 220\rangle^*$, which were equidistantly disposed along the directions parallel to $\langle 110\rangle^* L2_1$. As is known, they were due to the formation of the modulated martensite structure $10M$.

Cooling of the as-cast alloy to temperatures lower than room temperature led to the completion of TMT (Tables 2, 3). In this case, it turned that the regions of the retained austenite, as well as martensite crystals $10M$, underwent TMT to fine-lamellar martensite $14M$ (Fig. 7c). Their habits were also close to $\{110\}L2_1$. The microdiffraction patterns obtained from fine-lamellar martensite $14M$ (one of them is shown in Fig. 7d) contained rows of the 1/7(220)*-type extrareflections along certain directions (former $\langle 110^*\rangle L2_1$).

In the RQM alloy produced by spinning, the direct TMT took place in the temperature range 294–286 K (Tables 2, 3). Because of this, some of its features were gained even at room temperature in the fine-grained RQM alloy as compared to that in the initial as-cast coarse-grained alloy-prototype (Figs. 4–8). First, the grain-boundary mechanism of the $L2_1 \rightarrow 10M$ TMT was clearly revealed: grain boundaries were "decorated" with martensite crystals and, in addition, individual martensite plates and their packets going off out of them deep into grains were also observed (Figs. 8a, 8c, and 8e). During in situ cooling, TMT was completed in all grains with formation of twinned-in-pairs martensite $14M$ of one-packet morphology (Figs. 8b, 8d, and 8f). Thus, the $L2_1 + 10M$ alloy that was initially two-phase at room temperature underwent the two-stage austenite–martensite–martensite $L2_1 \rightarrow 10M \rightarrow 14M$ transformation, since, now, its microdiffraction patterns contained additional extrareflections of the 1/7(220)* type (Fig. 8f). However, the alloy contained, as before, individual wider untwined lamellar crystals of the tetragonal nonmodulated martensite NM ($c/a \sim 1.2$) that indicated by the arrow in Fig. 8d; the crystals can likely be retained on cooling.

The SEM method of electron back scattered diffraction (EBSD) and X-ray diffraction confirmed, as a whole, the TMT features in the as-cast and RQM alloys and their $L2_1 \leftrightarrow 10M \leftrightarrow 14M$ sequence (Figs. 9, 10). Unlike the case of the RQM alloy, the specific feature of the initial as-cast alloy was incomplete reversibility of this sequence on heating: $14M \leftrightarrow L2_1$. In addition, the micrograin structure of the RQM alloy had a strong cubic crystallographic texture, which was clearly seen from an analysis of the intensity ratio of the Bragg reflections of austenite and martensite in the RQM alloy (Fig. 10) and also from its EBSD images (Fig. 9).

Annealing of the RQM alloy at 1073 K (for 5 and 72 h) led not only to some increase in the grain sizes of the $L2_1$ austenite, but also to their equilibrium-faceted form (Figs. 4b–4d) and, as a result, to an increase in the plasticity of thin ribbons upon bending deformation and to an increase in the critical TMT temperatures to those slightly higher than room temperature. The one-packet character of the martensite morphology, as a whole, was conserved in the RQM alloy.

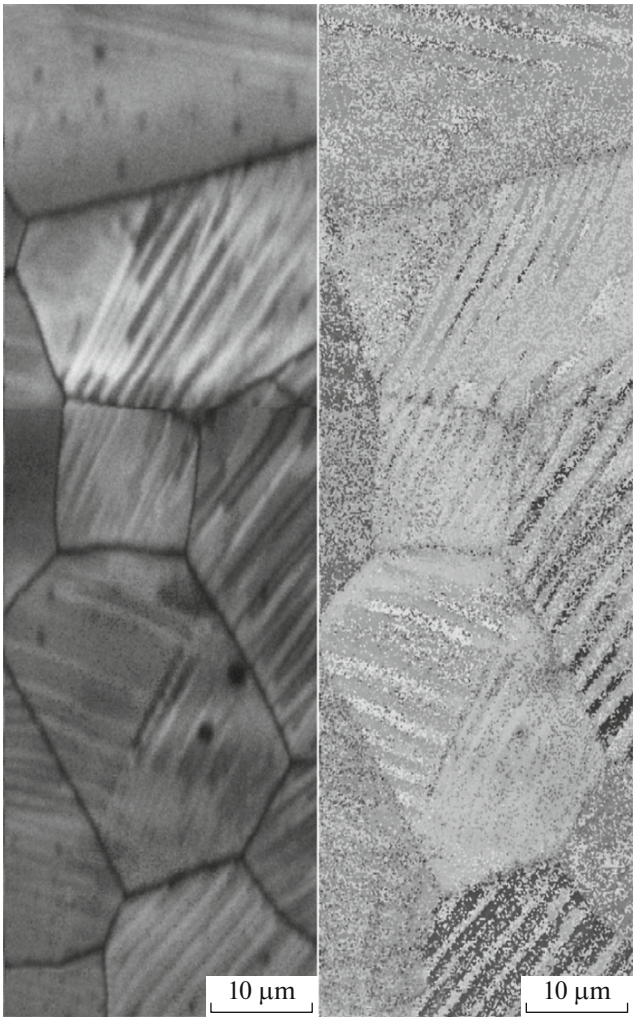

Fig. 9. Distribution maps of the twinned grained microstructure of the RQM alloy after annealing at a temperature of 1073 K for 72 h on their linear sizes and crystallographic orientations obtained by the SEM (EBSD) method. The discrete contrast of the microtwin structure (the right-side part of the figure) was due to a scanning pitch larger than linear sizes of thin secondary nanotwins.

7. CONCLUSIONS

Thus, as a result of the studies performed, it was found that the rapid quenching of the $Ni_{54}Mn_{21}Ga_{25}$ alloy, which caused substantial (by three orders) refinement of the grain microstructure, led to significant increase in the physicomechanical stability of the samples, their deformation thermal cyclic strength

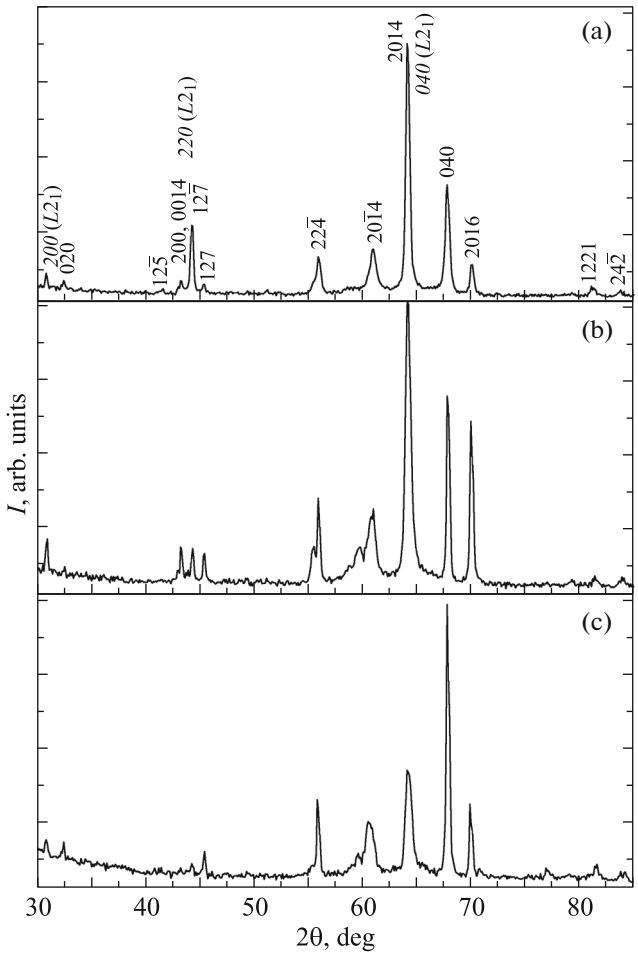

Fig. 10. X-ray diffraction patterns of the $Ni_{54}Mn_{21}Ga_{25}$ alloy with a strong crystallographic cubic texture of (italic) the retained $L2_1$ austenite inherited by the 14*M* martensite: (a) initial RQM state, (b, c) RQM alloy after annealing at 1073 K for 5 h and at 1073 K for 72 h, respectively.

and plasticity, despite some decrease in the degrees of atomic and magnetic orders. In this case, premartensite phenomena, the magnetic phase transition, high-reversible thermoelastic martensite transformations, and the related shape memory effects were conserved in full measure. In the rapidly quenched fine-grained alloy, the temperature hysteresis of the physical properties and the thermomagnetically controlled martensite transformation observed in the vicinity of the critical points decreased significantly, and it shifted to higher temperatures by 4–8 K in magnetic field H = 7.17 MA/m.

The thermoelastic martensite transformations in the initial as-cast alloy occurred in a wider temperature range and were not completely structure-reversible (no martensite 10*M* was observed on heating). The irreversible changes in the properties sensitive to them were a result of the structural–mechanical instability of the coarse-grain alloy with inherent chemical liquation that was dramatized by its high tendency to brittle fracture. There were almost not these irreversible changes in properties in the rapidly quenched fine-grained and chemically more homogeneous alloy.

A partial atomic disordering of the initial $L2_1$ structure in the rapidly quenched $Ni_{54}Mn_{21}Ga_{25}$ alloy led to the appearance of competing ferro- and antiferromagnetic interactions. At temperatures below T_C, this influenced the values and temperature dependences of the magnetic characteristics of the rapidly quenched alloy. At the same time, the degree of localization of the magnetic moment and other electron characteristics were almost not changed as a result of disordering of the collectivized magnet. This fact indicates the stability of the electron band structure near the Fermi level for the alloys produced by the two methods considered in this work.

ACKNOWLEDGMENTS

This work was supported by the Russian Foundation for Basic Research, project no. 15-12-10014.

The studies were performed using the analytical equipment of the Collective Use Center "Testing Center for Nanotechnologies and Advanced Materials" of the Institute of Metal Physics of Ural Branch of RAS.

REFERENCES

1. V. V. Kondrat'ev and V. G. Pushin, Fiz. Met. Metalloved. **60**, 629 (1985).
2. V. G. Pushin and V. V. Kondrat'ev, Fiz. Met. Metalloved. **78**, 40 (1994).
3. V. G. Pushin. Phys. Met. Metallogr. **90** (Suppl. 1), 68 (2000).
4. A. N. Vasil'ev, V. D. Buchel'nikov, T. Tagaki, V. V. Khovailo, and E. I. Estrin, Phys. Usp. **46**, 557 (2003).
5. V. N. Khachin, S. A. Muslov, V. G. Pushin, and Yu. I. Chumlyakov, Sov. Phys. Dokl. **32**, 606 (1987).
6. A. Zheludev, S. M. Shapiro, P. Wochner, and L. E. Tanner, Phys. Rev. B **54**, 15045 (1996).
7. L. Manoša, A. Planes, J. Zarestky, T. Lograsso, D. L. Schlagel, and C. Stassis, Phys. Rev. B **64**, 024305 (2001).
8. J. Worgull, E. Petti, and J. Trivisonno, Phys. Rev. B **54**, 15695 (1996).
9. P. J. Webster, K. R. A. Ziebeck, S. L. Town, and M. S. Peak, Philos. Mag. B **49**, 295 (1984).
10. V. A. Chernenko, C. Segui, E. Cesari, J. Pons, and V. V. Kokorin, J. Phys. IV (Fr.) **7**, C5-137 (1997).
11. J. Pons, V. A. Chernenko, R. Santa Marta, and E. Cesari, Acta Mater. **48**, 3027 (2000).
12. N. Lanska, O. Soderberg, A. Sozinov, Y. Ge, K. Ullakko, and V. K. Lindroos, J. Appl. Phys. **95**, 8074 (2004).
13. V. V. Kokorin and V. V. Martynov, Fiz. Met. Metalloved. **72**, 101 (1991).
14. M. Kreissl, K.-U. Neumann, T. Tephens, and K. R. A. Ziebeck, J. Phys.: Condens. Matter **15**, 3831 (2003).

15. N. I. Kourov, A. V. Korolev, V. G. Pushin, V. V. Koledov, V. G. Shavrov, and V. V. Khovailo, Phys. Met. Metallogr. **99**, 376 (2005).

16. N. I. Kourov, V. G. Pushin, A. V. Korolev, V. A. Kazantsev, E. B. Marchenkova, and A. N. Uksusnikov, Phys. Met. Metallogr. **103**, 270 (2007).

17. N. I. Kourov, V. V. Marchenkov, V. G. Pushin, A. V. Korolev, E. B. Marchenkova, and H. W. Weber, Phys. Solid State **50**, 2127 (2008).

18. N. I. Kourov, V. G. Pushin, A. V. Korolev, V. V. Marchenkov, E. B. Marchenkova, V. A. Kazantsev, and H. W. Weber, Phys. Solid State **53**, 91 (2011).

19. V. G. Pushin, N. I. Kourov, A. V. Korolev, E. B. Marchenkova, N. N. Kuranova, and E. S. Belosludtseva, Phys. Solid State **57**, 45 (2015).

20. A. V. Korolev, N. I. Kourov, and V. G. Pushin, Phys. Solid State **57**, 316 (2015).

21. Z. Wang, M. Matsumoto, S. T. Pantelides, K. Oikawa, J. Qiu, T. Takagi, and J. Tani, Mater. Sci. Forum **327–328**, 489 (2000).

22. S. V. Vonsovskii, *Magnetism* (Nauka, Moscow, 1971), [in Russian].

23. F. J. Blatt, *Theory of Mobility of Electrons in Solids* (Academic, New York, 1957).

Translated by Yu. Ryzhkov